DFT study of the fouling deposition process in the steam generator by simulating the absorption of Fe2+ on Fe3O4 (001)

Sanchuan Pan
Sun Yat-Sen University
Ren Lu (renlu@mail.sysu.edu.cn)
Sun Yat-Sen University
Jian Xu
Sun Yat-Sen University
Tetsuo Shoji
Tohoku University New Industry Creation Hatchery Center: Tohoku Daigaku Mirai Kagaku Gijutsu Kyodo Kenkyu Center
Ningning Li
Beijing University of Technology
Tong Zhang
Sun Yat-Sen University
Hongying Yu
Sun Yat-Sen University
Dongbai Sun
Sun Yat-Sen University

Research Article

Keywords: First principle, DFT, Fe3O4 (001) surface, Adsorption energy, Fouling, PWR

Posted Date: February 12th, 2021

DOI: https://doi.org/10.21203/rs.3.rs-213027/v1

DFT study of the fouling deposition process in the steam generator by simulating the absorption of Fe^{2+} on Fe_3O_4 (001)

Sanchuan Pan[a], Lu Ren[a, b, *], Jian Xu[a, b, *], Tetsuo Shoji[b], Ningning Li[c], Tong Zhang[a], Hongying Yu[a] and Dongbai Sun[a]

a School of Materials, Sun Yat-sen University, No.132, Outer-Ring East Road, Guangzhou 510006, P.R.China

b Frontier Research Initiative, New Industry Creation Hatchery Center, Tohoku University, 6-6-10 Aramaki Aoba, Aoba-ku, Sendai 980-8579, Japan

c College of Environmental and Energy Engineering, Beijing University of Technology, 100 Pingleyuan, Chaoyang District, Beijing 100124, P.R.China

Abstract: In this paper, the interaction between free Fe^{2+} and Fe_3O_4 corrosion products on the pipe surface in the secondary circuit of PWR nuclear power plant was studied, and the reason of agglomeration formation was analyzed. The complex physical and chemical interaction was simplified by describing the electron interaction. Based on the first principles, CASTEP was used to simulate seven kinds of highly symmetric adsorption structure models of Fe_{tet1} and Fe_{oct1} on Fe_3O_4 (001) surface, and their adsorption energies and stable adsorption conformations were calculated. The results show that the most stable adsorption structures of the Fe^{2+}/Fe_3O_4 (001) configurations are Fe_{oct1}-b and Fe_{tet1}-O_h. During the adsorption, the Fe-Fe, Fe-O bond length and Fe-Fe-O bond angle of (001) surface changed, and the atomic positions parallel and perpendicular to (001) surface changed correspondingly, the surface layer changes the most. The results prove that the adsorption has great effect on the physical structure of Fe^{2+} and Fe_3O_4 (001). The calculation of charge population, the density of states and

* Corresponding author: renlu@mail.sysu.edu.cn (Lu Ren), xujian3@mail.sysu.edu.cn (Jian Xu)

electron local function of Fe^{2+}/Fe_3O_4 (001) optimal adsorption configuration also shows that there is electron transfer between Fe^{2+} and Fe_3O_4 (001), and the adsorption type is chemisorption. Among them, Fe (Fe^{2+})-Fe (Fe_3O_4) forms a metal bond, and Fe (Fe^{2+})-O (Fe_3O_4) forms the ionic bond.

Keywords: First principle; DFT; Fe_3O_4 (001) surface; Adsorption energy; Fouling; PWR.

Declaration

Funding

Authors want to thank the support of the Guangdong Natural Science Foundation (2020A1515110449, 2020A1515011033), Foundation Research Funds for the Central Universities (19lgpy22), National Natural Science Foundation of China (51901254) and the start-up funding of the 100 talented program of Sun Yat-sen University (76180-18831103)

Conflicts of interest

The authors declare that they have no known competing financial interests or personal relationships that could have appeared to influence the work reported in this paper.

Availability of data and material

All data used during the study appear in the submitted article.

Code availability

Not applicable.

Authors' contributions

Sanchuan Pan: Conceptualization, Methodology, Resources, Writing - Original draft preparation. Lu Ren: Conceptualization, Methodology, Resources, Funding acquisition, Writing - review & editing. *Jian Xu:* Writing - review & editing. Tetsuo Shoji: Writing - review & editing. Ningning Li: Writing - review & editing. Tong Zhang: Writing - review & editing Hongying Yu: Writing - review & editing. Dongbai Sun: Writing - review & editing.

1 Introduction

The secondary heat exchange surface of steam generator (SG) in pressurized water reactor (PWR) of nuclear power plant (NPP) is easy to fouling, making the wing hole being gradually blocked by corrosion products[1]. The fouling phenomenon in SG secondary circuit was first found in Chalk River[2, 3]. The blocking phenomenon reduces the flow rate of the fluid passing through the supporting plate, and also increases the pressure drop, hinders the liquid passing through the secondary circuit, and reduces the heat exchange efficiency of SG[4]. When the blockage phenomenon becomes serious, the SG heat exchange tube and support plate will have strong vibration, and lead to fatigue fracture of the steam generator pipe. At present, several works proved that the majority of the fouling is in form of magnetite (Fe_3O_4)[1,5,6]

Fe_3O_4 has strong sub-magnetism and high electrical conductivity at room temperature, and widely used as a metal oxide catalyst. The fouling magnetite is composed of particle deposition and soluble ions in the medium. The soluble ions mainly come from the surface of materials dissolved in the secondary circuit. Moreover, the existence of Fe_3O_4 on the surface of SG heat exchange tube also has a certain adsorption effect on Fe^{2+} in the secondary circuit[7,8].

In order to analyze the interaction between Fe^{2+} and Fe_3O_4 surface in the agglomeration process, the density functional theory (DFT) was used for theoretical calculation[9-12]. At the same time, some studies involved the corresponding nanoscale model of corrosion fouling were carried out to find the most stable adsorption configuration of corrosion fouling in the protective layer and verified by molecular simulation[13, 14]. Fe_3O_4 is a kind of widely used oxide in industry, which has important catalytic performance[15-17]. The related research about the adsorption and dissociation of gas molecules on Fe_3O_4 surface provides a reference method for the interaction and agglomeration of Fe_3O_3

surface in the secondary circuit[18-20]. Yang et.al.[21] studied the surface structures of Fe_3O_4 (111), (110) and (001) by DFT method, and reasonably explained the diversity and complexity of the adsorption and catalytic properties of Fe_3O_4. Yin et.al.[22] used DFT method to analyze the behaviour of adding single-walled carbon nanotubes (SWNTs) to Fe_3O_4 nanoparticle electrodes, which can significantly improve the conductivity and performance of lithium-ion batteries. They believe that transition metal (Fe, Ni) atoms or clusters are helpful to form strong chemical bonds between SWNTs and Fe_3O_4 (001) surfaces, which provides a good channel for electrons and improve the conductivity. Xue et.al.[23] studied the adsorption characteristics of CO on the non-defect and defect (oxygen-containing vacancy) B-layer Fe_3O_4 (001) surface (octahedral environment) by using spin polarization DFT and Hubbard u parameter (DFT + U). They confirmed that both two types of B-layer Fe_3O_4 (001) surfaces had great CO oxidation ability. Yu et.al.[24] systematically analyzed the adsorption behaviour of CO on Fe_3O_4 (111), (110) and (001) surfaces, and analyzed the adsorption mechanism according to the projected density of states. Zhou et.al.[25] used DFT method to calculate the oxidation mechanism of Hg0 on Fe_3O_4 (001) surface by heterogeneous H_2O_2. The results show that the oxidation process may go through three different ways at the same time, and the mechanism may become an attractive method for mercury control in the flue gas. Therefore, the adsorption behaviour of particles on Fe_3O_4 (001) surface is affected by many factors, such as the structural electrification and surface integrity. At present, we can only find out that Fe^{2+} released by secondary side surface can adsorb on Fe_3O_4 surface, and lead to the continuous increase of Fe_3O_4 fouling in SG secondary circuit, but the relevant mechanism is still unclear.

In this paper, we simulate the deposition behaviour of Fe^{2+} on different terminals of (001) surface based on the first principles and find out the most stable adsorption configuration. We also analyze the adsorption structure characteristics and physical parameters and the adsorption behaviour characteristic.

The adsorption behaviour can be considered as the basis of the Fe_3O_4 deposition and agglomeration on the heat exchange tube secondary surface of the steam generator. In addition, by studying the geometry structure and adsorption energy of Fe^{2+} on Fe_3O_4 (001) surface, we can better understand the active electron properties, track the transfer direction of active electrons, and analyze the charge to describe the electronic properties of the most favourable adsorption configuration of Fe^{2+} on Fe_3O_4 (001) surface.

2 Computational methods and models

2.1 Methods

All the DFT calculations are performed using the Cambridge sequential total energy program package (CASTEP) module in the Materials Studio software package. The interaction between nucleus and electron is treated by ultra-soft pseudopotential. The generalized gradient approximation (GGA) parameterized by Perdew-Burke-Ernzerh (PBE) is used to describe the exchange correlation energy, and the plane wave basis set is used to expand the wave function[26-28], and the truncation energy is 450eV. In previous work, the magnetic properties of Fe_3O_4 have been confirmed by vibrating sample magnetometer (VSM), so the magnetic properties and the attached spin polarization of Fe_3O_4 have been considered in all calculations. To follow the principle of minimum energy, the spin from top to bottom of the unit cell is set as 4 and -4, described as Fe_{oct} and Fe_{tet}. The Fermi broadening of 0.1eV is used to accelerate the convergence. During Fe_3O_4 cell (space group Fd-3m/mmm) relaxing, the k-point in Brillouin zone is produced by Monkhorst-pack method, which is 3 × 3 × 1. In the relaxation process, when the maximum atomic force in any direction converges to 0.05eV/Å, the structural optimization is completed. The convergence criteria of self-consistent allowable error, energy, maximum displacement and maximum stress are set as 2.0×10−6eV/atom, 2.0×10^{-5}eV/atom, 0.00 Å and 0.1GPa. The lattice

constant of Fe_3O_4 crystal cell after optimization is a = b = c = 8.3942 Å, α = β = γ = 90°, which is close to the literature value (a = b = c = 8.394 Å, α = β = γ= 90°)[20].

The Fe_3O_4 crystal contains Fe^{2+} and Fe^{3+} and has a trans-spinel structure. The chemical formula can be written as $(Fe^{3+})_A(Fe^{3+}Fe^{2+})_BO_4$. There are 64 oxygen tetrahedral gaps (A sites) and 32 oxygen octahedral gaps (B sites). Among them, 1/8 A sites are occupied by Fe^{3+}, and 1/2 B sites are occupied by Fe^{2+} and Fe^{3+}. In Fe_3O_4, the sublattice containing tetrahedral oxygen gap is A-type sublattice, and the octahedral oxygen gap is B-type. The cell of Fe_3O_4 is formed by alternating stacking of A and B sublattices[20, 29-31].

In the SG secondary circuit of PWR, fouling deposit Fe_3O_4 have a low index surface (001) with higher symmetry, which has stable surface free energy in thermodynamics. Six nonequivalent ideal terminals can be obtained by cutting the Fe_3O_4 (001) stacking sequence. The terminals with fewer dangling bonds have higher stability. Therefore, the Fe_3O_4 (001) surfaces terminated by fetet1 and feoct1 can be regarded as the most stable terminals. The main content of this experiment is to explore the specific behaviour of fe_{tet1} and fe_{oct1} terminal configurations on Fe_3O_4 (001) surface in the secondary circuit[23].

By cutting (001), there are four terminals of stacking sequence, which are Fe_{tet1} and Fe_{tet2} with tetrahedral coordination Fe atoms exposed, Fe_{oct1} with exposed octahedral coordination Fe atoms and close packing O_{oct1} layer. The atomic plane stacking sequence perpendicular to (001) direction can be written as Fe_{oct1}- Fe_{tet1}-O_{oct1}-Fe_{tet2}. The (001) surface low index crystal surface of Fe_3O_4, with low Bragg index and high symmetry. In thermodynamics, the surface free energy of (001) surface is more favourable than that of natural growth surface (111), and its catalytic activity is consistent with (111)[32]. There will be different terminal faces after cleaving (001) surface, and the terminal surfaces with fewer dangling

bonds are relatively stable. That is, the Fe_{tet1} and Fe_{oct1}-terminal surface with the least dangling bonds are stable. Fe_{tet1}-terminal surface has one exposed tetrahedral Fe atom, and Fe_{oct1}-terminal surface two exposed octahedral Fe atoms and four exposed O atoms. Among these two kinds of terminal surfaces, the Fe_{oct1}-terminal surface is more likely to be the most active surface, because the exposed octahedral Fe atoms on this terminal surface have two valence states, which electrons can transition between them[21].

To analyze the stability of different adsorption configurations, we use the adsorption energy E_{AD} to compare the energy difference before and after adsorption. The formula is as follows:

$$E_{ad} = E_{Fe^{2+}/Fe_3O_4} - E_{Fe_3O_4} - E_{Fe^{2+}} \quad (1)$$

where E_{Fe^{2+}/Fe_3O_4} is the total energy of adsorbate and surface, $E_{Fe_3O_4}$ is the total energy of Fe_3O_4 (001) surface, and $E_{Fe^{2+}}$ is the total energy of isolated Fe^{2+}. When the adsorption energy is negative, it can be adsorbed, and the greater the absolute value, the easier the adsorption.

2.2 Models

Although Fe_{tet1}, O_{oct1}, Fe_{oct1}, and Fe_{tet2} can obtain nonequivalent ideal body termination by cutting Fe3O4 (001) stacking sequence, Fe_{tet1} and Fe_{oct1} terminals (as shown in Fig. 1) have only 6 bond breaks, and other terminations are more than this, so Fe_{tet1} and Fe_{oct1} terminals are stable. The Fe_{oct1}-terminal surface with exposed octahedral Fe atoms, as shown in Fig. 2, is selected as the model to study the secondary circuit reaction. Choosing the atomic model as the research object can achieve a good balance in precision and calculation time. The thickness of the vacuum layer is set at 15 Å to eliminate the periodic interaction. In the calculation process, the atoms at the bottom are fixed, and the atoms at the top two layers and adsorbate are allowed to relax.

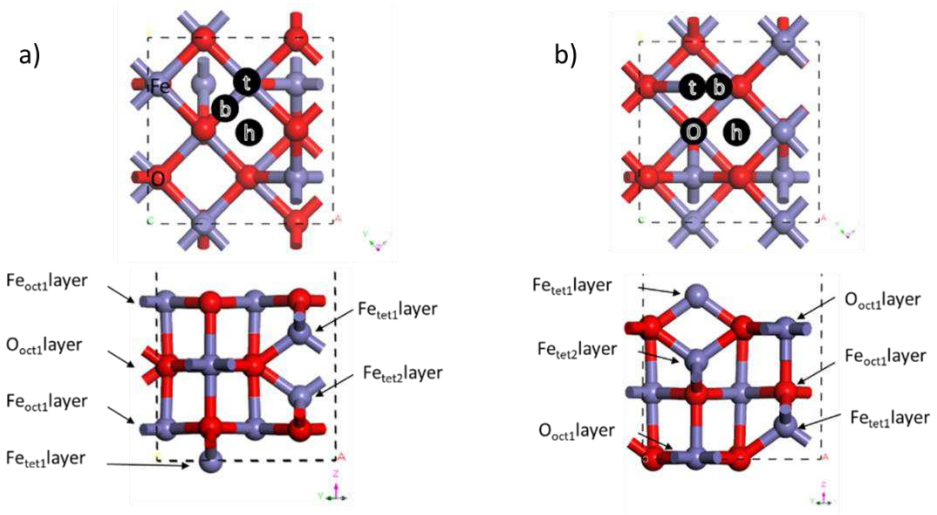

Fig. 1 Termination surface in a p (1×1) unit on Fe_3O_4 (001) surface after geometry optimization (a) Fe_{oct1} termination surface; (b) Fe_{tet1} termination surface

After geometry optimization, the partial density of states (PDOS) and energy band of Fe_{tet1} and Fe_{oct1} termination surfaces can be calculated, as shown in Fig. 2. The curves of PDOS show a similar trend, indicating that the two terminal surfaces have similar surface properties.

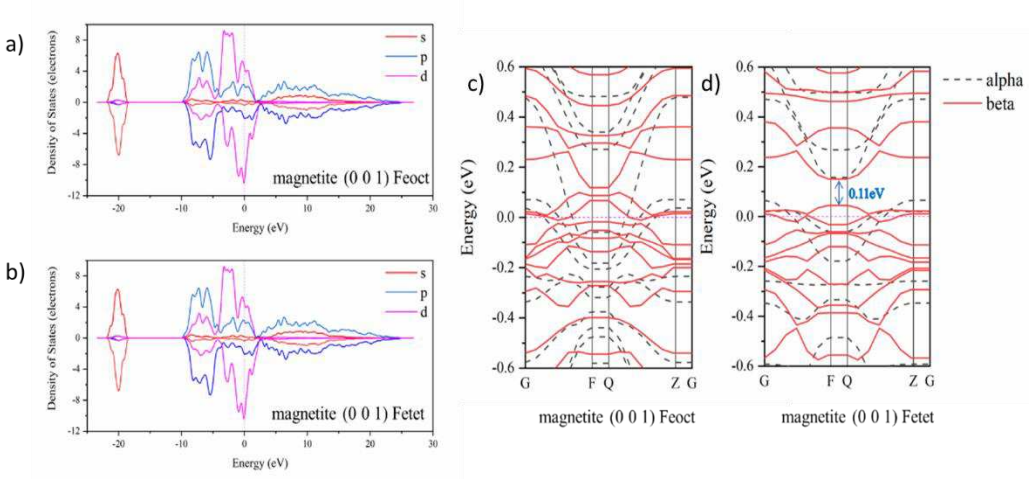

Fig. 2 Partial density of states (PDOS) and energy bands of Fe_{tet1} and Fe_{oct1} terminated surfaces on Fe_3O_4 (001) surface after geometry optimization: (a) PDOS on Fe_{oct1} termination surface; (b) PDOS on Fe_{tet1} termination surface; (c) energy band on Fe_{oct1} termination surface; (d) energy band on Fe_{tet1} termination surface

The local density of states of bulk structure includes the density of states of the nonequivalent atoms

Fe_{tet}, Fe_{oct} and O. the Fermi surface is represented by a straight line with zero energy. It can be seen from the TODS diagram of the bulk structure that the spin up and spin down subbands are divided into several parts, and there is no obvious band gap near the Fermi plane.

Through the calculation of the surface electronic structure of Fe_3O_4 (001), the DOS and energy band of Fe_{tet1} and Fe_{oct1} are given. POS includes TDOS, LPOS and PDOS, LDOS includes the density of states of Fe_{tet} and Fe_{oct} atoms, and PDOS includes the density of states of 3d orbital of Fe_{tet} and Fe_{oct} atoms. It can be found in TDOS that both spin-up and spin-down filled with electrons, which destroys the semi-metallicity. Similarly, the spin-up and spin-down sub-bands are divided into several parts, and no obvious band gap near the Fermi plane. Comparing the local density of states and the partial density of States, the spin-up electrons mainly occupy the 3d orbital of the surface Fe_{tet} atom and are highly localized near the Fermi plane, while the spin-down electrons occupy the d orbital near Fermi level. Both spin-up and spin-down are doped with a part of p orbitals of O atoms, and the density of states are also highly localized. The decrease of the coordination number of surface Fe ions may be the reason, and also lead to a decrease of sub-band gap and the instability of semi-metallicity.

In previous research, it had been concluded that the spin-down Fermi surface in PDOS diagram is mainly occupied by the electrons of Fe_{oct} atom and has a certain bandwidth, which leads to the semi-metallicity of Fe_3O_4 bulk structure [33, 34]. In the energy band diagram of Fe_{tet1}, we can find the 0.11eV spin-down bandgap, but no bandgap in the total density of states diagram. The bandgap indicates that the semi-metallicity of Fe_{tet1} surface exists, but it is not as strong as the original structure.

The high symmetry adsorptions sites are top (t), bridge (b) and hollow (h). According to the possible position of the highest adsorption energy and the high symmetry of Fe_3O_4 (001) surface, the following seven optimal adsorption points are listed: $Fe_3O_{4oct}^{(001)}$-t (Fe^{2+} above Fe_{oct}), $Fe_3O_{4oct}^{(001)}$-b (Fe^{2+} above Fe-O

bond), $Fe_3O_{4oct}^{(001)}$-h (Fe^{2+} above Fe-O bond), $Fe_3O_{4tet}^{(001)}$-t (Fe^{2+} above Fe_{tet}), $Fe_3O_{4tet}^{(001)}$-b site (Fe^{2+} above Fe-O bond), $Fe_3O_{4tet}^{(001)}$-O_h (Fe^{2+} above the hollow formed by O atoms) and $Fe_3O_{4tet}^{(001)}$-h (Fe^{2+} above the void formed by Fe and O). Figure 3 shows the front and top views of the corresponding configurations.

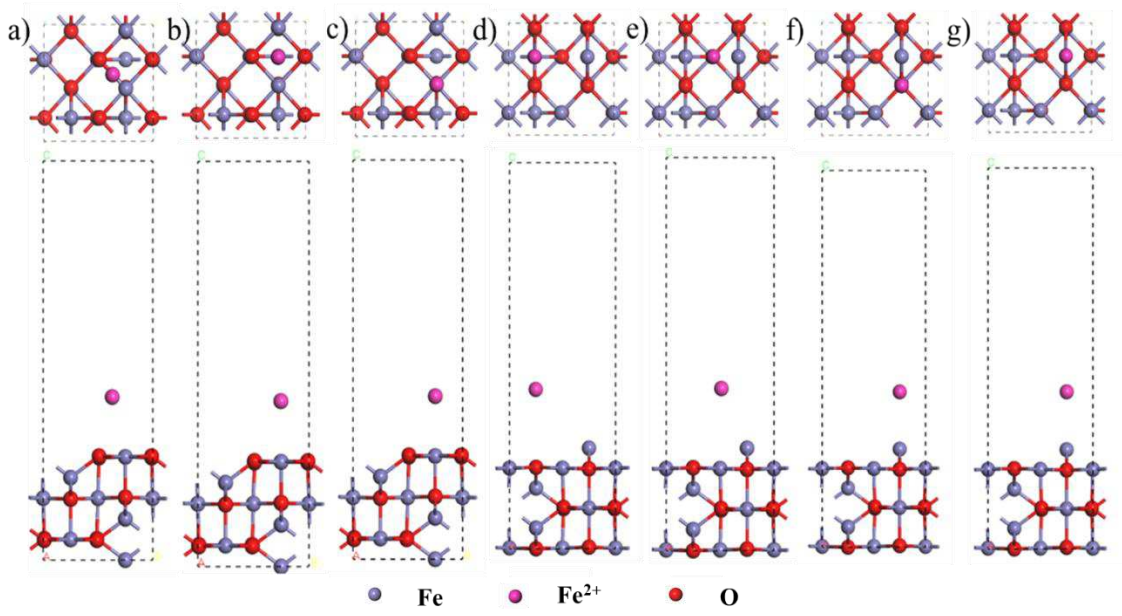

Fig. 3 Front view and top view of Fe^{2+} adsorption sites on Fe_3O_4 (001) surface(a) $Fe_3O_{4oct}^{(001)}$-t (b) $Fe_3O_{4oct}^{(001)}$-b (c) $Fe_3O_{4oct}^{(001)}$-h (d) $Fe_3O_{4tet}^{(001)}$-t (e) $Fe_3O_{4tet}^{(001)}$-b (f) $Fe_3O_{4tet}^{(001)}$-h (g) $Fe_3O_{4tet}^{(001)}$-O_h

3 Results and discussion

3.1 Adsorption structures and energy

The possible stable adsorption configuration of Fe^{2+} on Fe_3O_4(001) surface is shown in Fig. 4. The corresponding geometric structure parameters and adsorption energy can be seen in Table 1. The structure of Fe_3O_4(001) outmost surface may be affected by the adsorption behaviour of Fe^{2+}. The adsorption energy and the stable conformation of the system indicate that the most stable adsorption structure of Fe^{2+}/Fe_3O_4(001) surface are $Fe_3O_{4oct}^{(001)}$-b and $Fe_3O_{4tet}^{(001)}$-O_h site. After adsorption, Fe_{oct1}-O_{oct1}, Fe_{tet1}-O_{oct1} bond length and Fe_{oct1}-O_{oct1}-Fe_{tet1}, O_{oct1}-Fe_{tet1}-O_{oct1} bond angle change, varies from adsorption

configuration. $Fe_3O_{4oct}^{(001)}$-b and $Fe_3O_{4tet}^{(001)}$-O_h change the most. In $Fe_3O_{4oct}^{(001)}$-b configuration, Fe2+ bonds with both Fe atom and O atom of Fe_{oct1} termination surface, and have different bond length: Fe^{2+}-Fe(Fe_{oct1}) is 2.170 Å, Fe^{2+}-Fe(Fe_{tet1}) is 2.425 Å, and Fe^{2+}-Fe(O_{oct1}) is 2.526 Å. Should be noted that three Fe-Fe bonds have different electronic configurations, and will be further discussed later. Fe^{2+} bond with outmost Fe atom of Fe_{oct1}, such a behaver happen in al $Fe_3O_{4oct}^{(001)}$ configuration, meaning that Fe^{2+} affects the Oct1surface of Fe_3O_4 (001), and enables to bond with the nearest Fe atom. Similarly, the O atoms on Fe_{oct1} is also affected, and all of the $Fe_3O_{4\ oct}^{(001)}$ configuration have Fe2+-O(Fe_{oct1}). In $Fe_3O_{4\ tet}^{(001)}$ configuration, $Fe_3O_{4tet}^{(001)}$-t and $Fe_3O_{4tet}^{(001)}$-Fe_h have only one Fe^{2+}-Fe bond, but bonging Fe atoms have a different environment. $Fe_3O_{4tet}^{(001)}$-t one come from the outermost Fe_{tet1} layer, while $Fe_3O_{4tet}^{(001)}$-Fe_h one comes from the inner O_{oct1} layer. This result may be related to the distance between Fe^{2+} and different Fe atoms before the adsorption. From Table 1, we can know that $Fe_3O_{4oct}^{(001)}$-b is the largest adsorption energy site in $Fe_3O_{4oct}^{(001)}$ configuration, about -5.399eV the adsorption energy, while $Fe_3O_{4tet}^{(001)}$-O_h is the largest adsorption energy site in $Fe_3O_{4tet}^{(001)}$ configuration, about -4.599ev the adsorption energy. Compared the bonding conditions of the two configurations, it can be concluded that the more bonding one has the bigger adsorption energy, and the adsorption of Fe^{2+} on the surface of the Fe-O bond is more significant.

Table 1 Adsorption energy and structural parameters of Fe_3O_4 (001) at different adsorption sites

Substrate	terminal	Adsorption sites	E_{ad}/eV	$d_{Fe\text{-}O}$/Å	$d_{Fe\text{-}Fe}$/Å	bond angle/°
Fe_3O_4 (0 0 1)	Fe_{oct1}	$Fe_3O_{4oct}^{(001)}$-t	-1.799	2.238	2.095	51.700
		$Fe_3O_{4oct}^{(001)}$-b	-5.399	1.802;1.736	2.170;2.245; 2.526	49.402;94.737
		$Fe_3O_{4oct}^{(001)}$-h	-3.899	1.783;1.777	2.399;2.384	58.297;58.268
	Fe_{tet1}	$Fe_3O_{4tet}^{(001)}$-t	-2.599	---	2.015	87.641
		$Fe_3O_{4tet}^{(001)}$-O_t	-3.099	1.865	2.041	57.188
		$Fe_3O_{4tet}^{(001)}$-O_h	-4.599	1.790;1.784	2.218;2.409	50.090;52.237

$Fe_3O_4^{(001)}_{tet}$-Fe_h	-1.299	---	2.768	71.351

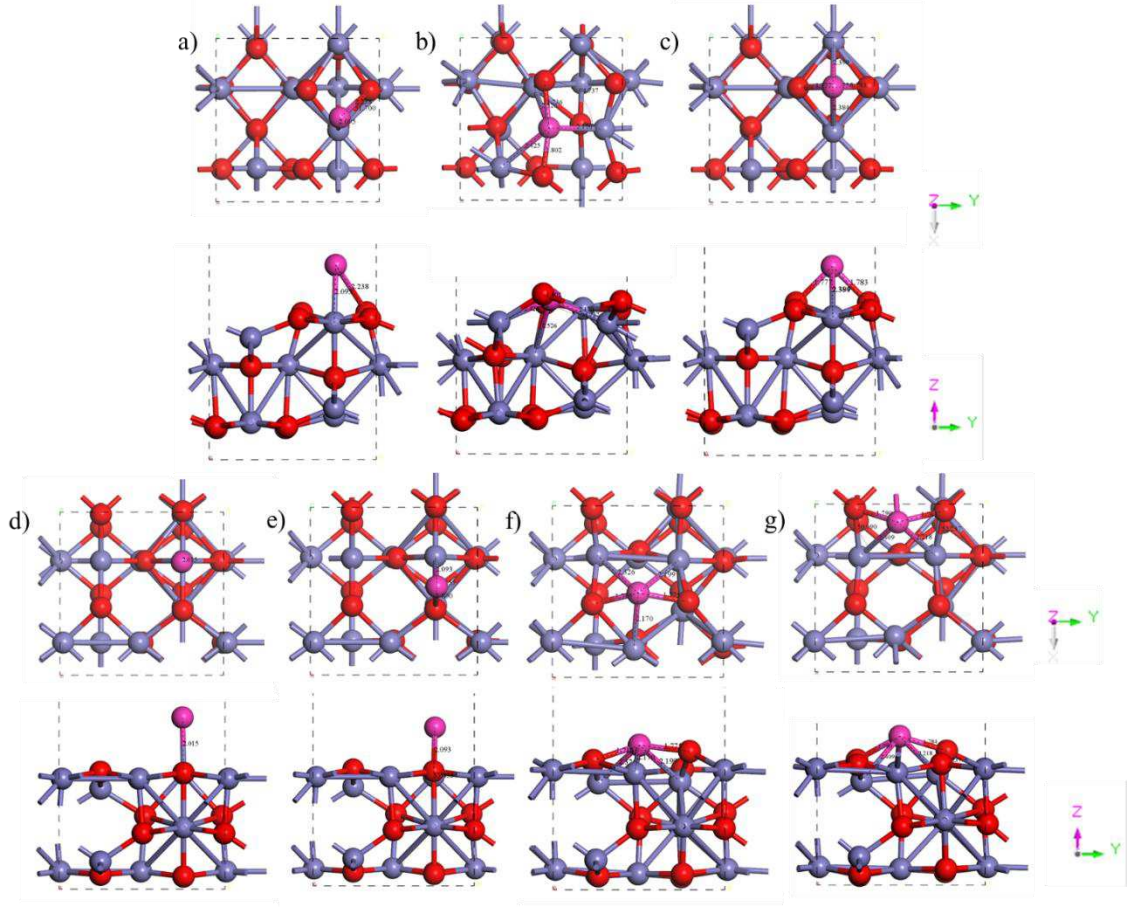

Fig. 4 Simulation results of Fe^{2+} adsorption on Fe_{tet1} and Fe_{oct1} terminated surfaces (a) Fe_3O_4 $^{(001)}_{oct}$-t (b) $Fe_3O_4^{(001)}_{oct}$-b (c) $Fe_3O_4^{(001)}_{oct}$-h (d) $Fe_3O_4^{(001)}_{tet}$-t (e) $Fe_3O_4^{(001)}_{tet}$-b (f) $Fe_3O_4^{(001)}_{tet}$-h (g) $Fe_3O_4^{(001)}_{tet}$-O_h

Fig. 5 shows the trajectories of $Fe_3O_4^{(001)}_{oct}$-b adsorption. Before adsorption, the Fe atom distances between Fe^{2+} and Fe_{oct1}, Fe_{tet1} and O_{oct1} are 3.204 Å, 5.165 Å and 5.252 Å, respectively. After 8ps relaxation, Fe^{2+} firstly forms a bond with Fe_{oct1}, and then desorb at 10ps due to the movement of the Fe atom. After 12ps of relaxation, Fe^{2+} reabsorbs and form a bond with 2.818 Å. At 54ps, a new Fe-Fe_{tet1} bond is formed due to the effect of Fe atoms in the Fe_{tet1} layer. In this process, the bond length of Fe-Fe_{oct1} is shortened to 2.120 Å. At 60ps, Fe^{2+} interacts with the Fe atom of O_{oct1} and bonds with it, the bond length is 2.883 Å, while Fe-Fe_{tet1} is shortened to 2.341 Å, Fe-Fe_{oct1} is elongated to 2.206 Å. The stretching of the Fe-Fe_{oct1} bond indicates that the new chemisorption bond is formed during the relaxation process, while the Fe-Fe_{oct1} is weakened, part of the electrons is transferred to the Fe-O_{oct1} bond. The

difference of Fe-Fe_{oct1}, Fe-Fe_{tet1} and Fe-O_{oct1} needs further analysis.

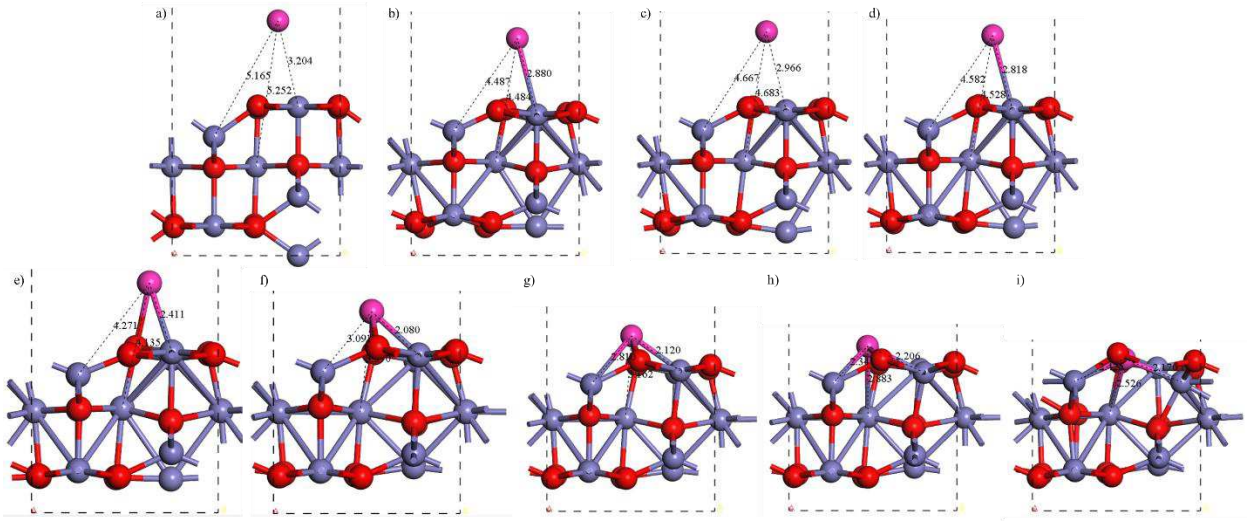

Fig. 5 Simulation outcome of $Fe_3O_4^{(001)}_{oct}$-b (a)1ps (b) 8ps (c) 10ps (d) 12ps (e) 24ps (f) 51ps (g) 54ps (h) 60ps (i) 75ps

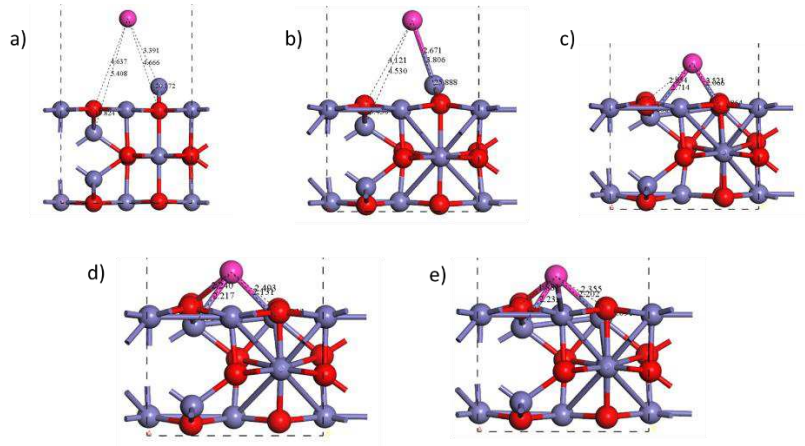

Fig. 6 Simulation outcome of $Fe_3O_4^{(001)}_{tet}$-O_h (a) 1ps (b) 16ps (c) 33ps (d) 37ps (e) 50ps

Fig. 6 shows the trajectory of $Fe_3O_4^{(001)}_{tet}$-O_h adsorption. Before adsorption, the distances between Fe^{2+} and the Fe atom of Fe_{tet1} and Fe_{tet2} layers are 3.391Å and 5.408 Å, respectively. After 16ps, Fe^{2+} is influenced by the outermost Fe atom in the Fe_{tet1} layer and bonding with each other. The bond length is gradually shortened and the electronic interaction is enhanced during relaxation. At 33ps, the Fe atoms in the Fe_{tet2} layer interact with Fe^{2+} and bonding, then this Fe-Fe_{tet2} bond continues to shorten in the relaxation process, while the Fe-Fe_{tet1} bond becomes lengthen in the relaxation process, meaning the

electronic interaction weakens. After 50ps, the bonding is stable. The bond length of Fe-Fe_{tet1} and Fe-Fe_{tet2} is 2.202 Å and 2.233 Å, respectively.

In conclusion, $Fe_3O_4^{(001)}_{oct}$-b is the most stable adsorption site of (001) surface. In the relaxation process, electron interaction can be found between Fe^{2+} and the surface, meaning that Fe^{2+} adsorption is chemisorption. This configuration has the most of chemical bonds and the highest adsorption energy.

3.2 Mulliken population

Table 2 Mulliken population of Fe^{2+} at different adsorption sites

Substrate	Terminal	Adsorption sites	q_{o1}/eV	q_{o2}/eV	q_{fe1}/eV	q_{fe2}/eV	q_{fe2+}/eV
Fe_3O_4(0 0 1)	Fe_{oct1}	$Fe_3O_4^{(001)}_{oct}$-t	0.14	0.11	0.18	---	0.43
		$Fe_3O_4^{(001)}_{oct}$-b	0.48	0.39	0.21	-0.13	0.95
		$Fe_3O_4^{(001)}_{oct}$-h	0.38	0.39	0.02	0.04	0.83
	Fe_{tet1}	$Fe_3O_4^{(001)}_{tet}$-t	-0.02	-0.03	0.63	---	0.58
		$Fe_3O_4^{(001)}_{tet}$-Fe_h	---	---	0.16	---	0.16
		$Fe_3O_4^{(001)}_{tet}$-O_h	0.34	0.32	0.13	0.12	0.91
		$Fe_3O_4^{(001)}_{tet}$-O_t	0.24	---	0.29	---	0.53

As shown in Table 2, the maximum Mulliken charge of Fe^{2+} is 0.95eV of $Fe_3O_4^{(001)}_{oct}$-b and 0.91eV of $Fe_3O_4^{(001)}_{tet}$-O_h, both of them are positive, indicating that electrons transfer from Fe_3O_4 (001) surface to Fe^{2+}. Analyzing the changes of Mulliken charge population and bond population before and after adsorption, the bonding strength between Fe^{2+} and Fe_3O_4 (001) surface, the electronic configuration, and further the characteristics of electron exchange between Fe^{2+} and Fe_3O_4 (001) surface can be obtained. The higher Mulliken charge can be observed on Fe_{oct1} terminal surface, which because of the higher prominent molecular polarity on Fe_{tet1} terminal surface, making the bonding atoms contribute less charge. $Fe_3O_4^{(001)}_{oct}$-b configuration has the largest adsorption energy, about -5.399eV, and its Mulliken charge value is also the largest among all configurations. Therefore, the charge distribution of Fe_3O_4 (001) surface can be understood by analyzing the Mulliken charge value of $Fe_3O_4^{(001)}_{oct}$ -b adsorption site. The above calculation results show that when Fe^{2+} is adsorbed on Fe_3O4 (001) surface, the adsorbed Fe^{2+} is the

acceptor and absorb electrons from the Fe_{oct1} and Fe_{tet1} terminal surface.

Table 3 Mulliken population of $Fe_3O_4^{(001)}_{oct}$-b configuration

Species	Spin	Mulliken population (before adsorption)/e					Mulliken population (after adsorption)/e				
		s	p	d	Charge(e)	Spin(hbar/2)	s	p	d	Charge(e)	Spin(hbar/2)
O1		0.94	2.41		-0.64		0.94	2.45		-0.65	
O2		0.93	2.42		-0.67		0.94	2.37		-0.65	
O3		0.94	2.41		-0.63		0.94	2.49		-0.67	
O4		0.93	2.42		-0.67		0.93	2.41		-0.67	
O5		0.94	2.37		-0.58		0.94	2.34		-0.57	
O6		0.94	2.42		-0.64		0.94	2.43		-0.64	
O7		0.94	2.41		-0.63		0.93	2.40		-0.63	
O8		0.94	2.37		-0.58		0.94	2.40		-0.62	
O9		0.93	2.42		-0.67		0.93	2342		-0.66	
O10		0.93	2.42		-0.67		0.93	2.37		-0.64	
O11		0.93	2.44		-0.63		0.94	2.45		-0.65	
O12		0.93	2.44		-0.63		0.94	2.44		-0.63	
Fe1	up:	0.14	0.19	4.27	0.77	2.09	0.26	0.22	4.65	0.82	3.07
	dn:	0.12	0.12	2.31			0.15	0.13	1.77		
Fe2	up:	0.16	0.18	1.87	0.82	-2.69	0.15	0.25	1.89	0.74	-2.70
	dn:	0.13	0.22	4.48			0.16	0.23	4.54		
Fe3	up:	0.17	0.23	1.77	0.68	-2.92	0.13	0.23	1.79	0.80	-2.88
	dn:	0.14	0.28	4.60			0.16	0.28	4.59		
Fe4	up:	0.15	0.24	4.30	0.63	2.06	0.18	0.26	4.68	0.66	2.90
	dn:	1.15	0.26	2.21			0.15	0.28	1.80		
Fe5	up:	0.15	0.24	4.31	0.99	2.04	0.17	0.23	4.38	0.63	2.19
	dn:	0.15	0.27	2.25			0.16	0.26	2.17		
Fe6	up:	0.20	0.18	4.38	0.92	2.51	0.19	0.25	2.50	0.57	-1.54
	dn:	0.14	0.15	1.95			0.19	0.24	4.05		
Fe7	up:	0.21	0.18	4.42	0.92	2.53	0.18	0.18	4.55	1.00	2.81
	dn:	0.15	0.15	1.98			0.13	0.16	1.81		
Fe8	up:	0.19	0.19	4.58	0.92	5.83	0.19	0.16	4.43	0.87	2.43
	dn:	0.15	0.17	1.81			0.15	0.15	2.05		
Fe9	up:	0.19	0.18	4.58	0.92	2.82	0.19	0.19	4.69	0.97	3.12
	dn:	0.15	0.16	1.81			0.15	0.17	1.63		
Fe10	up:						0.24	0.11	2.30	0.61	-2.10
	dn:						0.29	0.10	4.35		

Table 3 shows the Mulliken charge population of $Fe_3O_4^{(001)}_{oct}$-b site before and after adsorption.

Compared the values before and after adsorption, the charge population of each atom in the matrix

changes stably. Fe^{2+} mainly obtains the surface electrons of Fe_3O_4 (001) through 3d orbitals, 2.30e in spin-up and 4.35e in spin-down. Fe2, Fe4 and Fe6 atoms which bonded with Fe^{2+} show the electron numbers change in p and d orbitals. The spin-up electrons of Fe2 and Fe4 decrease, and spin-down electrons increase. In Fe6, however, have reverse phenomenon, which spin-up electrons increase and spin-down electrons decrease. These results show that the bonding mechanism of Fe2, Fe4 and Fe6 with Fe^{2+} is different, and may make a different influence on the electronic configuration of the adsorbed surface. The change of the electrons number indicates that there is electron transition between Fe^{2+} and Fe_3O_4 (001) surface, and further proves that the interaction between Fe^{2+} and atoms on Fe_3O_4 (001) surface include electron transfer and chemical bond formation when Fe^{2+} is adsorbed on $Fe_3O_{4oct}^{(001)}$-b site.

Table 4 shows the changes of bond population and bond length after adsorption on $Fe_3O_{4oct}^{(001)}$-b site. It can be seen from Table 4 that the newly formed bond O2-Fe10 population is 0.39e and the bond length is 1.801 Å; bond O8-Fe10 population number is 0.48e and the bond length is 1.736 Å. The Fe-O bond length of the matrix is between 1.577 μ and 2.268 μ, which indicates that the newly formed Fe-O bond can be regarded as the extension of the matrix, and O2 and O8 atoms make a great effect to Fe^{2+}, which can be regarded as the existence of electric field effect, meaning the new Fe-O bond is an ionic bond. Besides, the populations of Fe2-Fe10, Fe4-Fe10 and Fe6-Fe10 formed after adsorption are 0.05, 0.21 and - 0.13, respectively, and the bond lengths are 2.242 Å, 2.525 Å and 2.170 Å, respectively, meaning that the interaction between Fe4 and Fe^{2+} is strong, while the influence of Fe2 and Fe6 is weak. The negative population indicates that the electron is transferred from Fe^{2+} to Fe10 on Fe6-Fe10, so the bonding behaviour of Fe^{2+} is much more complex.

Table 4 Population and length of chemical bond of $Fe_3O_4^{(001)}_{oct}$-b site

Bond	Population/e	Spin	Length/Å	Bond	Population/e	Spin	Length/Å
O8-Fe10	0.48	0.04	1.7362	O4-Fe8	0.34	-0.03	1.884
O5-Fe6	0.51	0.04	1.7852	O4-Fe9	0.36	-0.04	1.885
O4-Fe3	0.49	0.06	1.7907	O9-Fe9	0.35	-0.04	1.887
O10-Fe6	0.43	0.02	1.8002	O11-Fe2	0.37	0.05	1.888
O2-Fe10	0.39	0.01	1.8018	O12-Fe5	0.33	-0.02	1.890
O9-Fe3	0.5	0.06	1.812	O7-Fe3	0.35	0.04	1.902
O12-Fe2	0.44	0.06	1.824	O5-Fe7	0.32	-0.03	1.914
O3-Fe1	0.43	-0.02	1.830	O3-Fe8	0.32	-0.01	1.934
O5-Fe5	0.4	-0.02	1.830	O1-Fe8	0.29	-0.01	1.937
O6-Fe3	0.45	0.07	1.834	O7-Fe1	0.23	-0.05	1.947
O2-Fe7	0.38	-0.04	1.8393	O12-Fe4	0.3	-0.03	1.952
O10-Fe7	0.38	-0.05	1.842	O1-Fe5	0.28	0	1.955
O10-Fe2	0.4	0.04	1.843	O6-Fe1	0.19	-0.05	1.964
O2-Fe2	0.38	0.04	1.854	O11-Fe9	0.2	-0.06	1.985
O1-Fe1	0.41	-0.02	1.855	O12-Fe8	0.18	-0.06	1.996
O9-Fe8	0.35	-0.03	1.873	O11-Fe5	0.25	-0.03	2.001
O8-Fe7	0.32	-0.03	1.875	O11-Fe4	0.26	-0.04	2.016
O7-Fe6	0.38	0.03	1.876	O 6-Fe 7	0.21	-0.06	2.037
O8-Fe4	0.41	-0.03	1.882	O 3-Fe 9	0.27	-0.02	2.039

In conclusion, after Fe^{2+} adsorbs on Fe_3O_4 (001) surface, there is an electron exchange and new chemical bond formation between Fe^{2+} and Fe_3O_4 (001) surface. Electron exchange between Fe atoms and Fe^{2+} form metal bonds, while electron exchange between O atoms and Fe^{2+} form an ionic bond. According to the analysis of the Mulliken population and bond population, Fe_3O_4 (001) surface can adsorb Fe^{2+} in PWR nuclear power plant secondary circuit and create new chemical bonds, which is also the reason for the continuous deposition of Fe_3O_4 surface particles. This is also consistent with the conclusion.

3.3 Electronic density of states

To analyze the electronic density of states of different bonding formed at adsorption sites, the PDOS of $Fe_3O_4^{(001)}_{oct}$-b configuration after adsorption is made, as shown in Fig. 7, so the comprehensive changes of bonding conditions, adsorption energy and electronic density of states can be studied.

Comparing the PDOS diagram of the $Fe_3O_{4oct}^{(001)}$-b configuration with that of Fe_{oct1} termination face before adsorption, it is observed that the charge change mainly occurs in the 3d orbit, and the 3d orbit of Fe^{2+} has a hybrid orbital peak near the Fermi level. The 3d resonance of Fe^{2+} spin-up electrons occurs at Fermi level indicates that the spin-up electrons can only be partially filled and the adsorption is characterized by a covalent bond. However, the 3d resonance of the spin-down electrons mainly occurs below the Fermi level, about -3eV, indicates that Fe^{2+} is mainly affected by negative ions during the adsorption. At the same time, the broadening of spin-up and spin-down p-orbital electrons at 4ev is also increasing, which enhances the p-orbital hybridization. However, there are no s-and p-orbital hybridization characteristics of O atom at this place, meaning that Fe^{2+} has little effect from the O atom of Fe_3O_4. Therefore, the agglomeration process is mainly affected by the 3d orbital of the Fe atom and has a covalent bond effect. However, a small peak included 3s, 3p and 3d orbitals appear at -20ev in the PDOS diagram of Fe^{2+}, while only the 2s orbit of O has a high electron peak here, which means that in $Fe_3O_{4oct}^{(001)}$-b configuration, the 2s orbital of O atom will participate in the orbital hybridization of Fe^{2+} and affect the bonding, but the effect is not as great as that of 3d orbital of Fe atom.

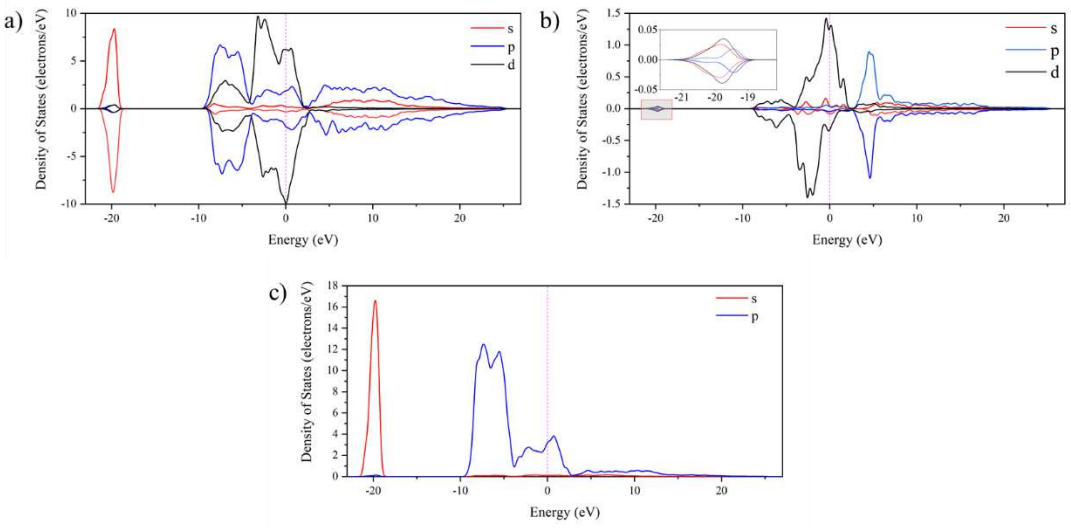

Fig. 7 PDOS after Fe^{2+} is absorbed at $Fe_3O_{4oct}^{(001)}$-b site (a) $Fe_3O_{4oct}^{(001)}$-b (b) Fe^{2+} in $Fe_3O_{4oct}^{(001)}$-b

configuration (c) O atom in $Fe_3O_4^{(001)}_{oct}$-b configuration

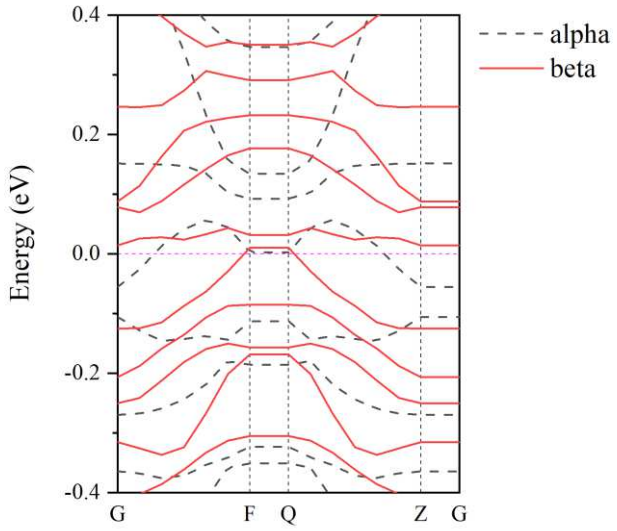

Fig. 8 Energy band diagram of $Fe_3O_4^{(001)}_{oct}$-b configuration

The energy band diagram of $Fe_3O_4^{(001)}_{oct}$-b configuration is shown in Fig. 8. Compared with Fig. 8 and Fig. 3c, the fluctuation of Fe^{2+} after adsorption at $Fe_3O_4^{(001)}_{oct}$-b site tends to be gentle, indicates that electron localization is weakened and the surface charge distribution is uniform, which may due to the effect of Fe^{2+} bonding with multiple surface Fe atoms and O atoms. It can be observed that the spin-up and spin-down sub-bands are divided into several parts, and the bandgap near the Fermi plane is small. Comparing the local density of states and the partial density of states, we can found that the electrons near the Fermi surface occupy the 3d orbits of the surface Fe atoms, and the electrons are highly localized near the Fermi surface. When Fe^{2+} relaxes on the Fe_3O_4 (001) surface, the formation of Fe-Fe bond makes the adsorption surface show the characteristics of Fe_3O_4 (001) surface and shows strong metallicity, which is similar to the previous calculation. The active metal bond leads to electrons appear in the forbidden band, and the surface charge is evenly distributed, which makes it easier for Fe_{2+} to become a new part of Fe_3O_4 surface after adsorption, accelerates the agglomeration process and

enhances the matrix effect.

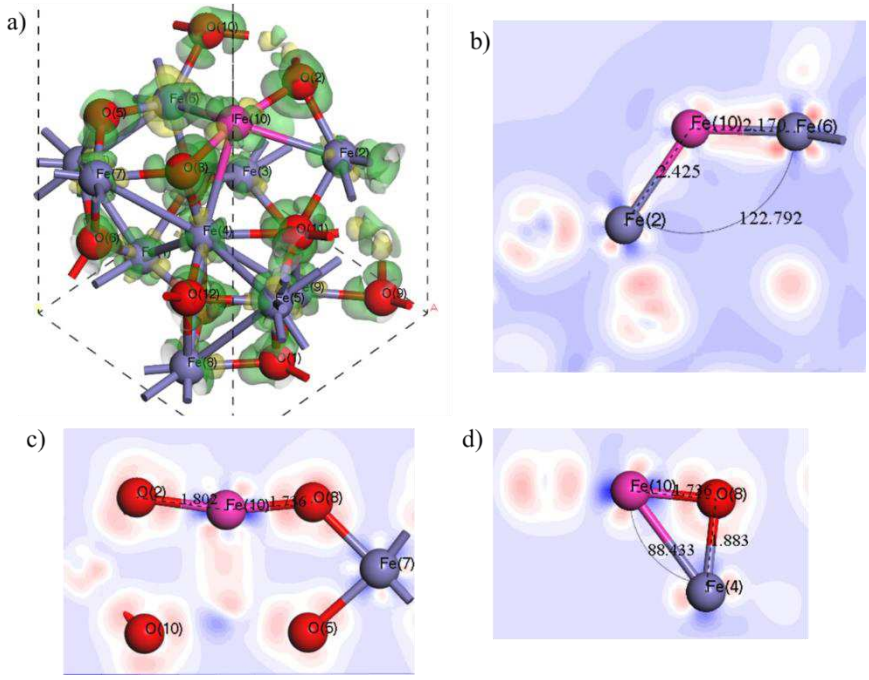

Fig. 9 Differential electron density diagram of $Fe_3O_4^{(001)}_{oct}$-b configuration (a) differential electron density diagram (b) local electron distribution of Fe2-Fe^{2+}-Fe6 (c) local electron distribution of O2-Fe^{2+}-O8 (d) local electron distribution of O8-Fe^{2+}-Fe4

For further analysis about the electron localized behaviour of Fe^{2+} on the $Fe_3O_4^{(001)}_{oct}$-b site, as shown in Fig.9, the differential electron density diagram is used to directly describe the redistribution of surface electrons after relaxation. We definite $\Delta\rho = \rho(Fe^{2+}/Fe_3O_4) - \rho(Fe^{2+}) - \rho(Fe_3O_4)$, varies from $-0.9e^{-3}$ to $1.0e^{-3}$. The red area means electron enrichment and the blue area means electron depletion. It can be seen that on Fe_3O_4 (001) surface, obvious charge transfer exists between Fe^{2+}-Fe. The change of charge density is the largest, leading to new bonding between atoms, and finally, form a stable chemisorption configuration. In the diagram, Fe^{2+} and Fe6 atoms have electron interaction, and the electron density increases, indicating that a great overlap covalent bond exists between them, which can be considered as σ bond. At the same time, fig.9c also shows electron interaction between Fe^{2+} and Fe2, but the electron localization is not as large as that of Fe^{2+}-Fe6, and the orbital overlap is low, indicates that the covalent

bond formed should be β bond. The d electron localization of Fe^{2+}-Fe4 is even lower than that of Fe^{2+}-Fe2, so have a weaker β covalent bond. It can be found through the electronic localization that the density of electron cloud around Fe6 is more negative than that of Fe^{2+} after Fe6 is bonded with Fe^{2+}, and the bonding condition of Fe6 is different from Fe2 and Fe4. According to the different electronegativity, Fe^{2+} may form a bond with Fe6 by giving electrons, and after bonding, Fe6 feedback some electrons to Fe^{2+}, which makes the electronic localization of Fe^{2+}-Fe6 increase. Also, the electron interaction between Fe^{2+} and the nearby O atoms increases with the decrease of the distance, forming new Fe-O bonds. The charge density of the O atom is high, have maximized electrostatic interaction with Fe^{2+}. The rearrangement of these charges will lead to the activation of the Fe-O bond and become ionic bond structure.

4 Conclusion

Fe^{2+} adsorption on the surface of the nuclear power plant steam generator secondary circuit heat transfer tube will agglomerate the fouling and accelerate the scaling process through the electron interaction. Through the first-principles calculation, we simulated the changes of Fe_3O_4 (001) surface before and after adsorption. It is found that all the atom positions of Fe_3O_4 crystal parallel to and perpendicular to (001) surface change, and the outmost surface layer changes the most, which means that the adsorption has great influence on the physical structure of Fe^{2+} and Fe_3O_4 (001) crystals. This article also studies the charge population, density of States and electron local function of Fe^{2+}/Fe_3O_4 (001) adsorption system. The calculation shows that there is electron transfer between Fe^{2+} and Fe_3O_4 (001) to form a chemical bond. Among them, Fe (Fe^{2+}) - Fe (Fe_3O_4) forms a metal bond, and Fe (Fe^{2+}) - O (Fe_3O_4) forms the ionic bond. The formation of Fe (Fe^{2+}) - Fe (Fe_3O_4) metal bond leads to the electronic state in the forbidden band, which may be the reason why Fe^{2+} adsorbs on the surface of Fe_3O_4 (001) and

enhances the matrix effect.

Acknowledgements

Authors want to thank the support of the Guangdong Natural Science Foundation (2020A1515110449, 2020A1515011033), Foundation Research Funds for the Central Universities (19lgpy22), National Natural Science Foundation of China (51901254) and the start-up funding of the 100 talented program of Sun Yat-sen University (76180-18831103)

Declaration of interests

The authors declare that they have no known competing financial interests or personal relationships that could have appeared to influence the work reported in this paper.

References:

1. Yang GZ, Pointeau V, Tevissen E, Chagnes A (2017) A review on clogging of recirculating steam generators in Pressurized-Water Reactors. Progress in Nuclear Energy 97:182-196. doi:10.1016/j.pnucene.2017.01.010

2. Cassineri S, Duff J, Cioncolini A, Curioni M, Banks A, Scenini F (2019) Deposition of corrosion products under pressurised water nuclear reactor conditions: The effect of flow velocity and dissolved hydrogen. Corros Sci 159. doi:ARTN 10811310.1016/j.corsci.2019.108113

3. McGrady J, Scenini F, Duff J, Stevens N, Cassineri S, Curioni M, Banks A (2017) Investigation into the effect of water chemistry on corrosion product formation in areas of accelerated flow. Journal of

Nuclear Materials 493:271-279. doi:10.1016/j.jnucmat.2017.06.030

4. Cong TL, Tian WX, Qiu SZ, Su GH (2013) Study on secondary side flow of steam generator with coupled heat transfer from primary to secondary side. Applied Thermal Engineering 61 (2):519-530. doi:10.1016/j.applthermaleng.2013.08.024

5. Cissé S, Laffont L, Tanguy B, Lafont M-C, Andrieu E (2012) Effect of surface preparation on the corrosion of austenitic stainless steel 304L in high temperature steam and simulated PWR primary water. Corros Sci 56:209-216. doi:10.1016/j.corsci.2011.12.007

6. Jeon S-H, Choi W-I, Song G-D, Son Y-H, Hur D (2016) Influence of Surface Roughness and Agitation on the Morphology of Magnetite Films Electrodeposited on Carbon Steel Substrates. Coatings 6 (4). doi:10.3390/coatings6040062

7. Bansal B, Chen XD, Müller-Steinhagen H (2008) Analysis of 'classical' deposition rate law for crystallisation fouling. Chemical Engineering and Processing: Process Intensification 47 (8):1201-1210. doi:10.1016/j.cep.2007.03.016

8. Fujiwara K, Domae M, Yoneda K, Inada F (2011) Model of physico-chemical effect on flow accelerated corrosion in power plant. Corros Sci 53 (11):3526-3533. doi:10.1016/j.corsci.2011.06.027

9. Striolo A, Bratko D, Wu JZ, Elvassore N, Blanch HW, Prausnitz JM (2002) Forces between aqueous nonuniformly charged colloids from molecular simulation. Journal of Chemical Physics 116 (17):7733-7743. doi:10.1063/1.1467343

10. Qin Y, Fichthorn KA (2003) Molecular-dynamics simulation of forces between nanoparticles in a Lennard-Jones liquid. Journal of Chemical Physics 119 (18):9745-9754. doi:10.1063/1.1615493

11. Kadota K, Furukawa R, Shirakawa Y, Shimosaka A, Hidaka J (2014) Effect of surface properties of calcium carbonate on aggregation process investigated by molecular dynamics simulation. J Mater Sci

49 (4):1724-1733. doi:10.1007/s10853-013-7859-7

12. Kadota K, Furukawa R, Tozuka Y, Shimosaka A, Shirakawa Y, Hidaka J (2014) Formation mechanism of non-spherical calcium carbonate particles in the solution using cluster-moving Monte Carlo simulation. J Mol Liq 194:115-120. doi:10.1016/j.molliq.2014.01.019

13. Kaya S, Banerjee P, Saha SK, Tuzun B, Kaya C (2016) Theoretical evaluation of some benzotriazole and phospono derivatives as aluminum corrosion inhibitors: DFT and molecular dynamics simulation approaches. Rsc Adv 6 (78):74550-74559. doi:10.1039/c6ra14548e

14. Saha SK, Ghosh P, Hens A, Murmu NC, Banerjee P (2015) Density functional theory and molecular dynamics simulation study on corrosion inhibition performance of mild steel by mercapto-quinoline Schiff base corrosion inhibitor. Physica E 66:332-341. doi:10.1016/j.physe.2014.10.035

15. Kheilkordi Z, Ziarani GM, Badiei A, Vojoudi H (2020) A green method for the synthesis of indeno[1,2-b]pyridines using Fe3O4@SiO2@PrSO3H as a nanomagnetic catalyst. Iran J Catal 10 (1):65-70

16. Jiang LT, Chen JF, An Y, Han DQ, Chang S, Liu Y, Yang RN (2020) Enhanced electrochemical performance by nickel-iron layered double hydroxides (LDH) coated on Fe3O4 as a cathode catalyst for single-chamber microbial fuel cells. Sci Total Environ 745. doi:ARTN 14116310.1016/j.scitotenv.2020.141163

17. Chen WH, Huang JR, Lin CH, Huang CP (2020) Catalytic degradation of chlorpheniramine over GO-Fe 3 O 4 in the presence of H 2 O 2 in water: The synergistic effect of adsorption. Sci Total Environ 736. doi:ARTN 13946810.1016/j.scitotenv.2020.139468

18. Meng Y, Liu X-Y, Bai M-M, Chen J, Ma Y-J, Wen X-D (2020) Adsorption or deoxidation of H2 interacted with Fe3O4 surface under different H coverage: A DFT study. Appl Surf Sci 502.

doi:10.1016/j.apsusc.2019.144097

19. Yu X, Zhang X, Jin L, Feng G (2017) CO adsorption, oxidation and carbonate formation mechanisms on Fe3O4 surfaces. Phys Chem Chem Phys 19 (26):17287-17299. doi:10.1039/c7cp02760e

20. Zhou C, Song Z, Zhang Z, Yang H, Wang B, Yu J, Sun L (2017) DFT studies of elemental mercury oxidation mechanism by gaseous advanced oxidation method: Co-interaction with H 2 O 2 on Fe 3 O 4 (111) surface. Appl Surf Sci 426:647-655. doi:10.1016/j.apsusc.2017.07.243

21. Yang T, Wen X-d, Ren J, Li Y-w, Wang J-g, Huo C-f (2010) Surface structures of Fe3O4 (111), (110), and (001): A density functional theory study. Journal of Fuel Chemistry and Technology 38 (1):121-128. doi:10.1016/s1872-5813(10)60024-2

22. Yin WJ, Wei SH, Ban CM, Wu ZC, Al-Jassim MM, Yan YF (2011) Origin of Bonding between the SWCNT and the Fe3O4(001) Surface and the Enhanced Electrical Conductivity. Journal of Physical Chemistry Letters 2 (22):2853-2858. doi:10.1021/jz201277s

23. Xue PY, Fu ZM, Chu XL, Zhang YX, Yang ZX (2014) Density functional theory study on the interaction of CO with the Fe3O4(001) surface. Appl Surf Sci 317:752-759. doi:10.1016/j.apsusc.2014.09.002

24. Yu X, Jin L, Zhao C, Liu Z (2019) High Coverage CO Adsorption on Fe6O6 Cluster Using GGA + U. Journal of Cluster Science 31 (3):591-600. doi:10.1007/s10876-018-1485-0

25. Zhou C, Yang H, Qi D, Sun J, Chen J, Zhang Z, Mao L, Song Z, Sun L (2018) Insights into the heterogeneous Hg0 oxidation mechanism by H2O2 over Fe3O4 (0 0 1) surface using periodic DFT method. Fuel 216:513-520. doi:10.1016/j.fuel.2017.12.004

26. Yang T, Wen XD, Huo CF, Li YW, Wang J, Jiao H (2009) Structure and energetics of hydrogen adsorption on Fe3O4(111). Journal of Molecular Catalysis a-Chemical 302 (1-2):129-136.

doi:10.1016/j.molcata.2008.12.009

27. Merte LR, Olsson PAT, Shipilin M, Gustafson J, Bertram F, Zhang C, Gronbeck H, Lundgren E (2020) Structure of two-dimensional Fe3O4. J Chem Phys 152 (11):114705. doi:10.1063/1.5142558

28. Ren L, Cheng Y, Shao R, Meng X, Yang J, Wang Q (2020) DFT studies of adsorption properties and bond strengths of H2S, HCN and NH3 on Fe(1 0 0). Appl Surf Sci 500. doi:10.1016/j.apsusc.2019.144232

29. Li X, Paier J, Sauer J, Mirabella F, Zaki E, Ivars-Barcelo F, Shaikhutdinov S, Freund HJ (2018) Surface Termination of Fe3O4(111) Films Studied by CO Adsorption Revisited. J Phys Chem B 122 (2):527-533. doi:10.1021/acs.jpcb.7b04228

30. Roldan A, Santos-Carballal D, de Leeuw NH (2013) A comparative DFT study of the mechanical and electronic properties of greigite Fe3S4 and magnetite Fe3O4. J Chem Phys 138 (20):204712. doi:10.1063/1.4807614

31. Mariotto G, Murphy S, Shvets IV (2002) Charge ordering on the surface of Fe3O4(001). Physical Review B 66 (24). doi:ARTN 24542610.1103/PhysRevB.66.245426

32. Santos-Carballal D, Roldan A, Grau-Crespo R, de Leeuw NH (2014) A DFT study of the structures, stabilities and redox behaviour of the major surfaces of magnetite Fe3O4. Physical Chemistry Chemical Physics 16 (39):21082-21097. doi:10.1039/c4cp00529e

33. Fonin M, Pentcheva R, Dedkov YS, Sperlich M, Vyalikh DV, Scheffler M, Rudiger U, Guntherodt G (2005) Surface electronic structure of the Fe3O4(100): Evidence of a half-metal to metal transition. Physical Review B 72 (10). doi:ARTN 10443610.1103/PhysRevB.72.104436

34. Mounkachi O, Lamouri R, Hamedoun M, Ez-Zahraouy H, Salmani E, Benyoussef A (2017) Effect of Defects Disorder on the Half-Metallicity, Magnetic Properties, and Gap States of Fe3O4: a First-

Principles Study. Journal of Superconductivity and Novel Magnetism 30 (11):3221-3224. doi:10.1007/s10948-017-4108-3

Figures

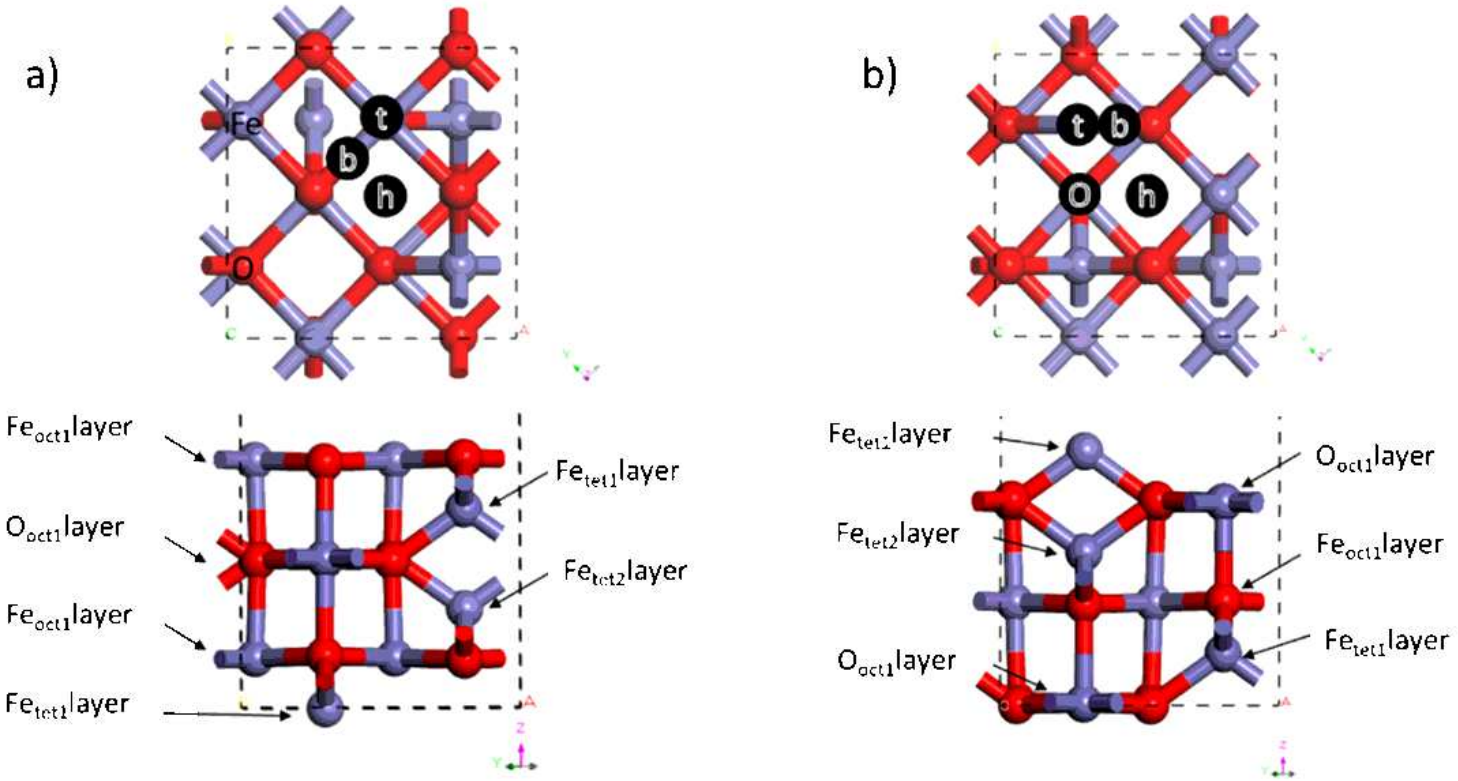

Figure 1

Please see the Manuscript Doc file for the complete figure caption.

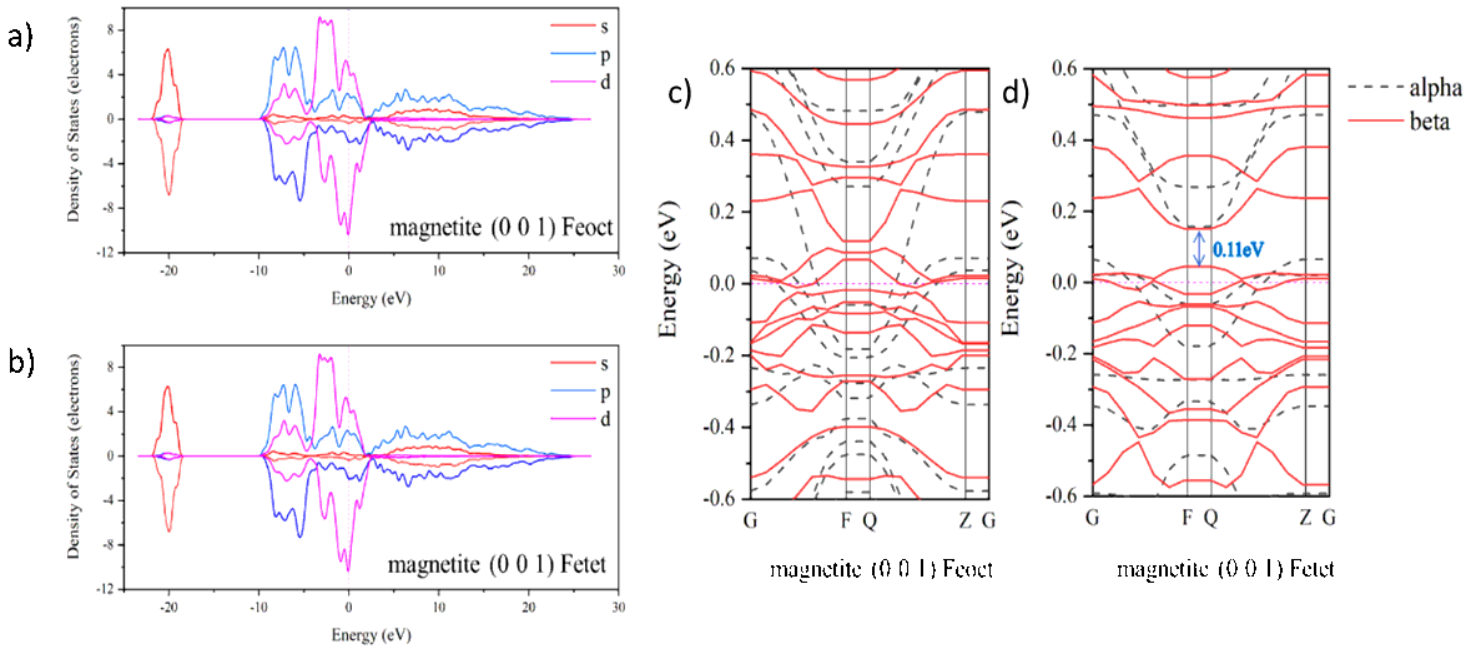

Figure 2

Please see the Manuscript Doc file for the complete figure caption.

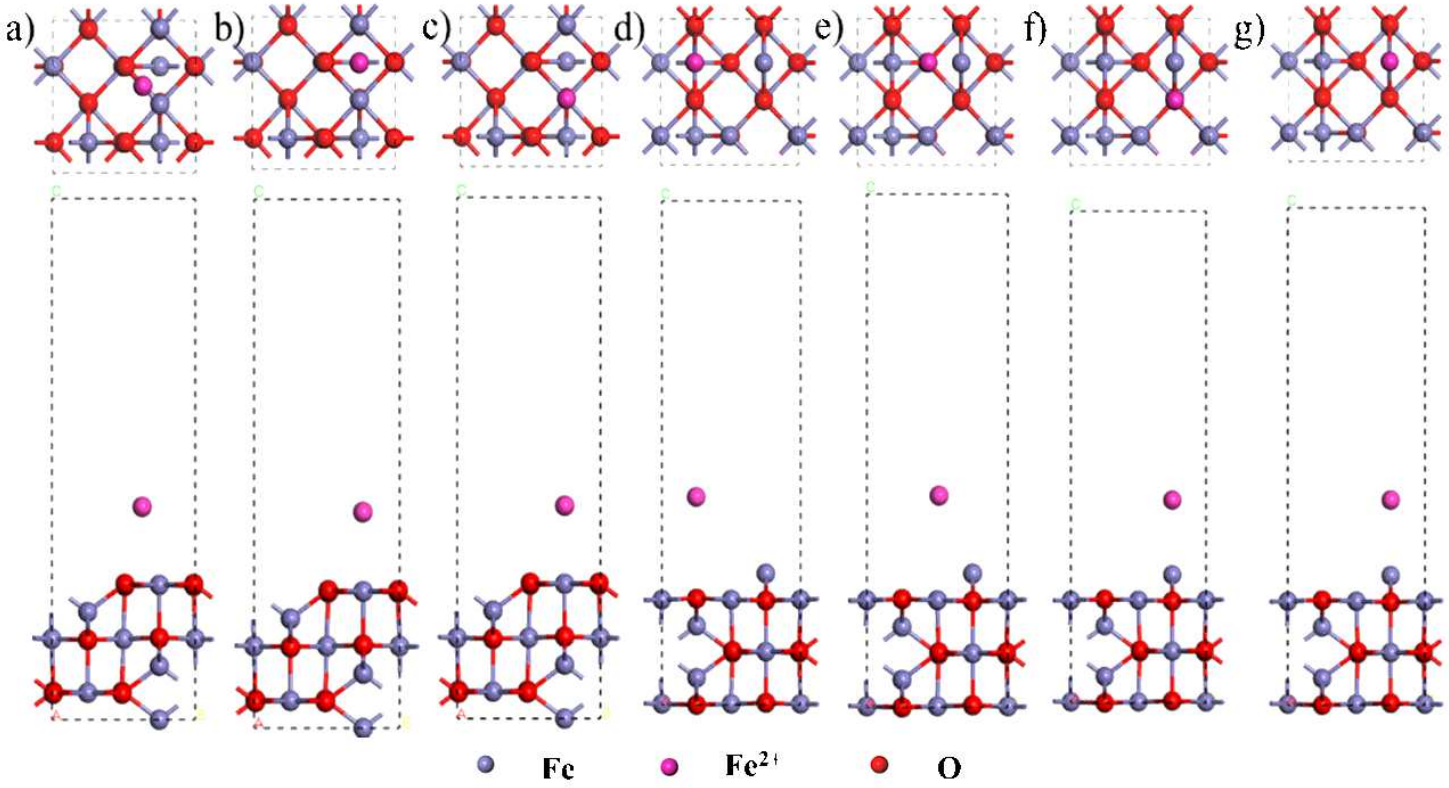

Figure 3

Please see the Manuscript Doc file for the complete figure caption.

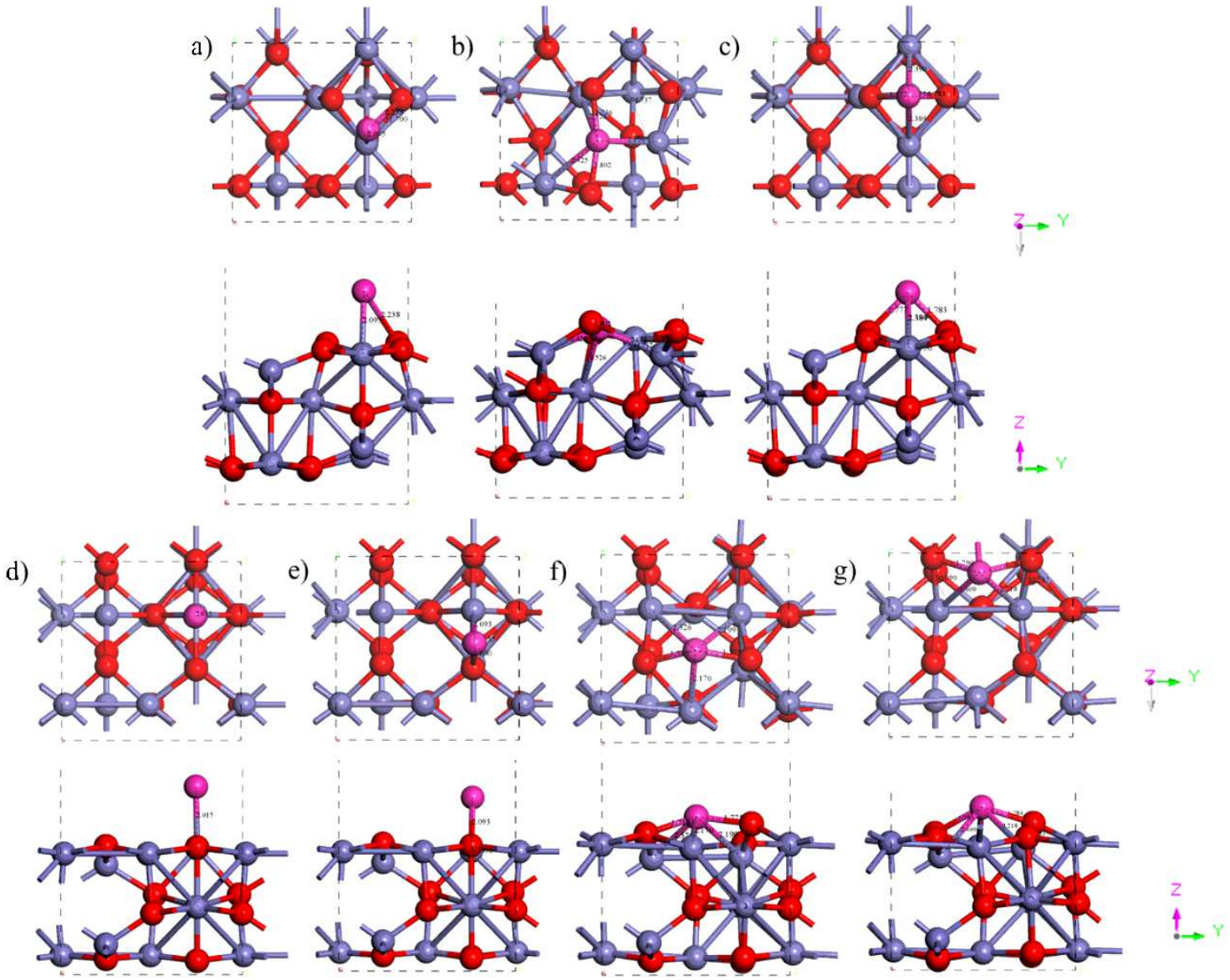

Figure 4

Please see the Manuscript Doc file for the complete figure caption.

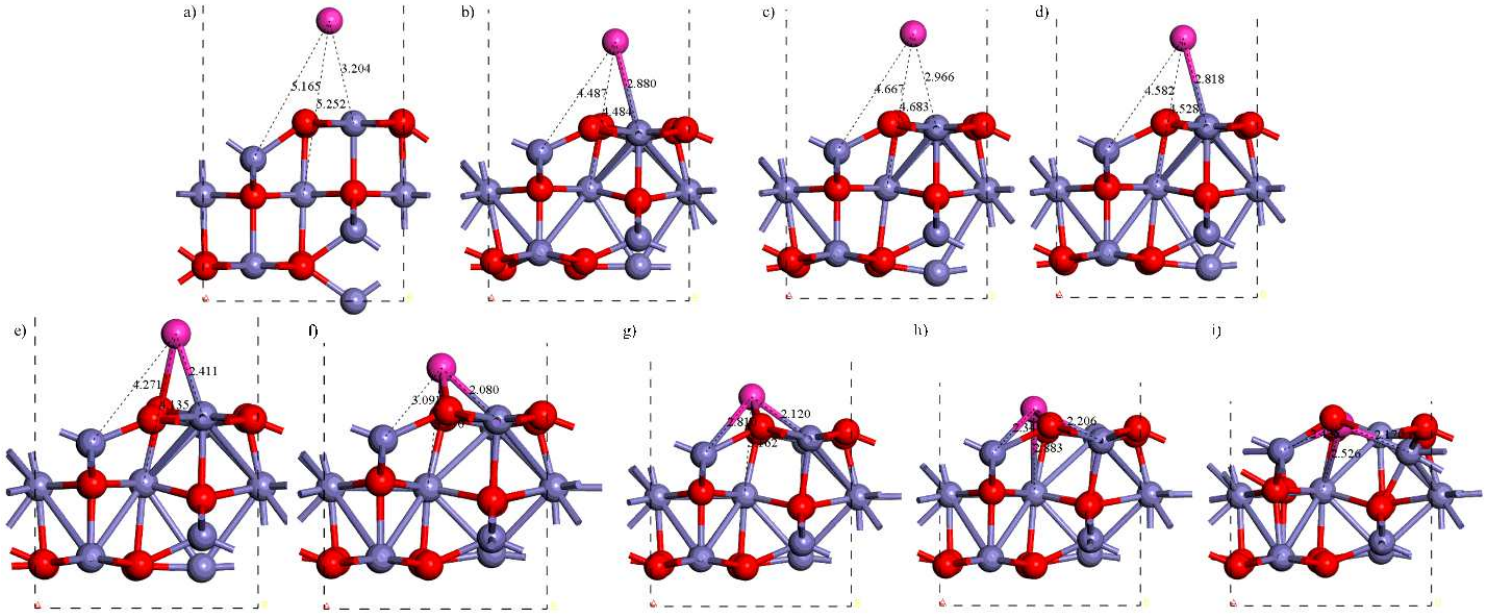

Figure 5

Please see the Manuscript Doc file for the complete figure caption.

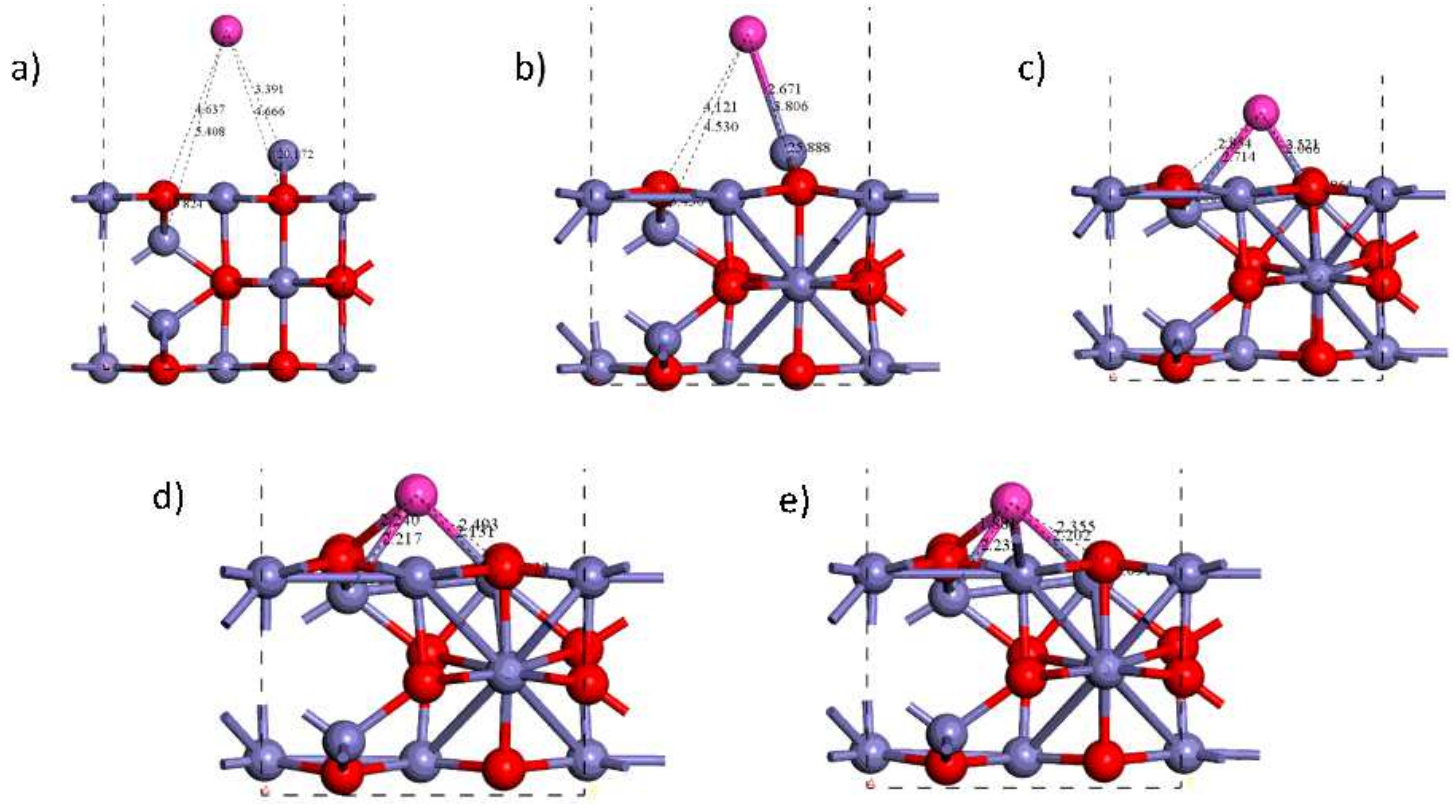

Figure 6

Please see the Manuscript Doc file for the complete figure caption.

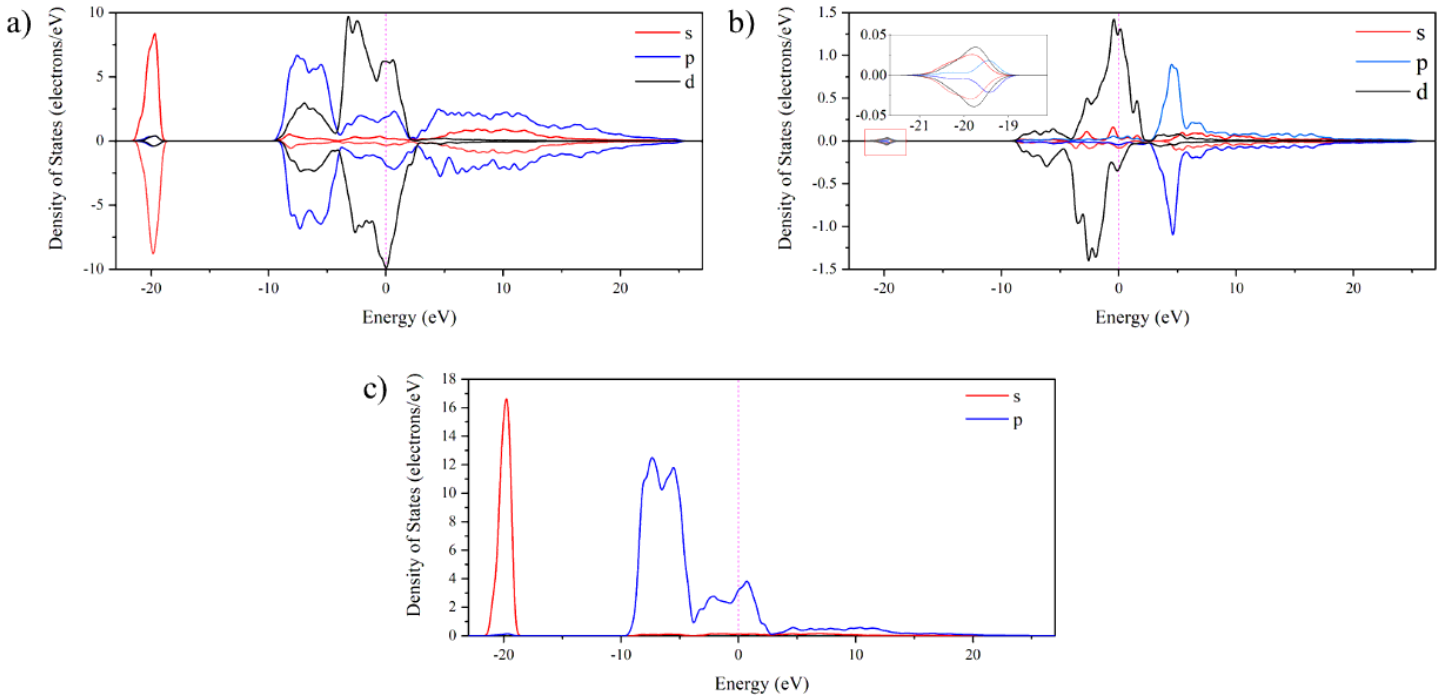

Figure 7

Please see the Manuscript Doc file for the complete figure caption.

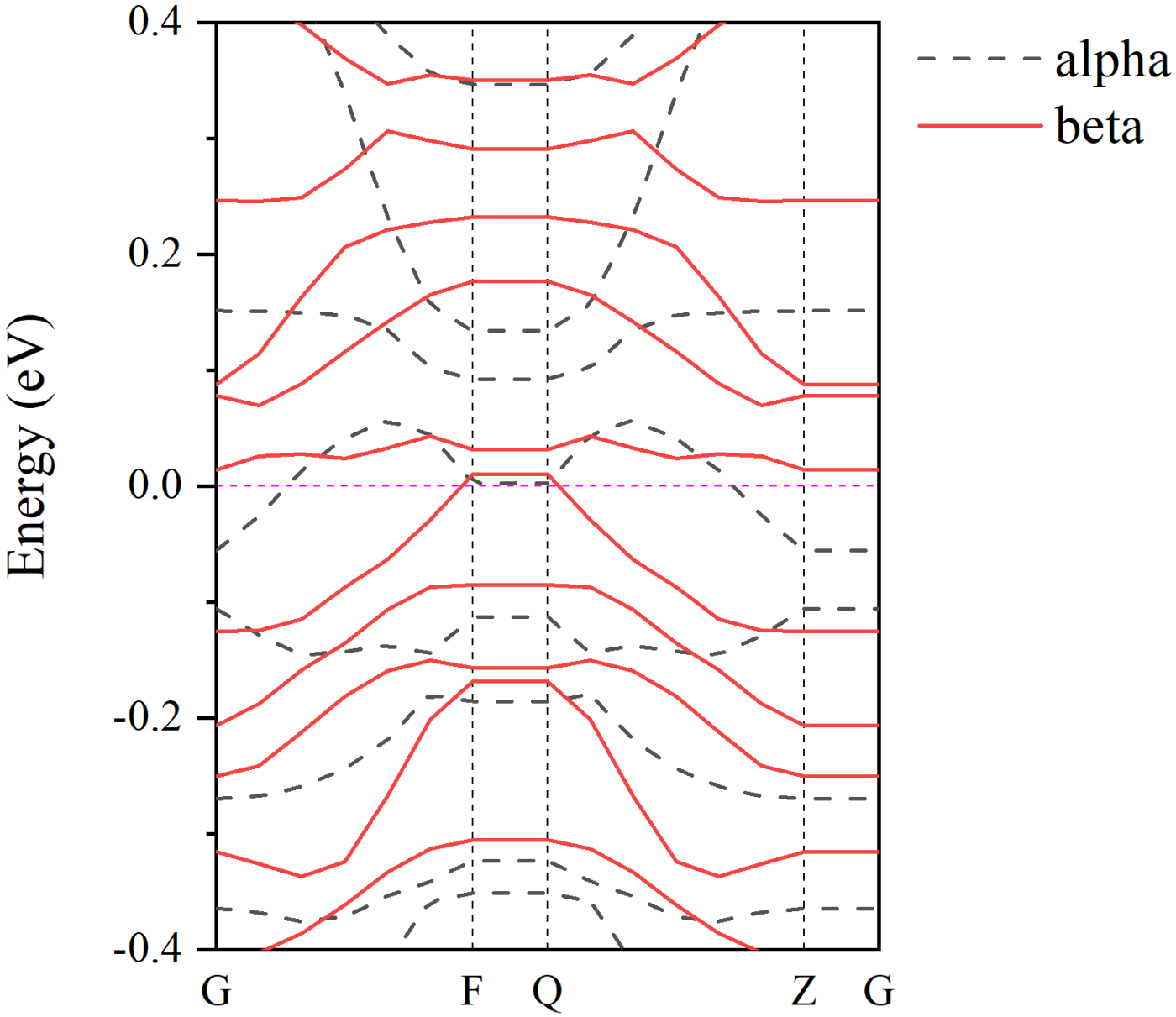

Figure 8

Please see the Manuscript Doc file for the complete figure caption.

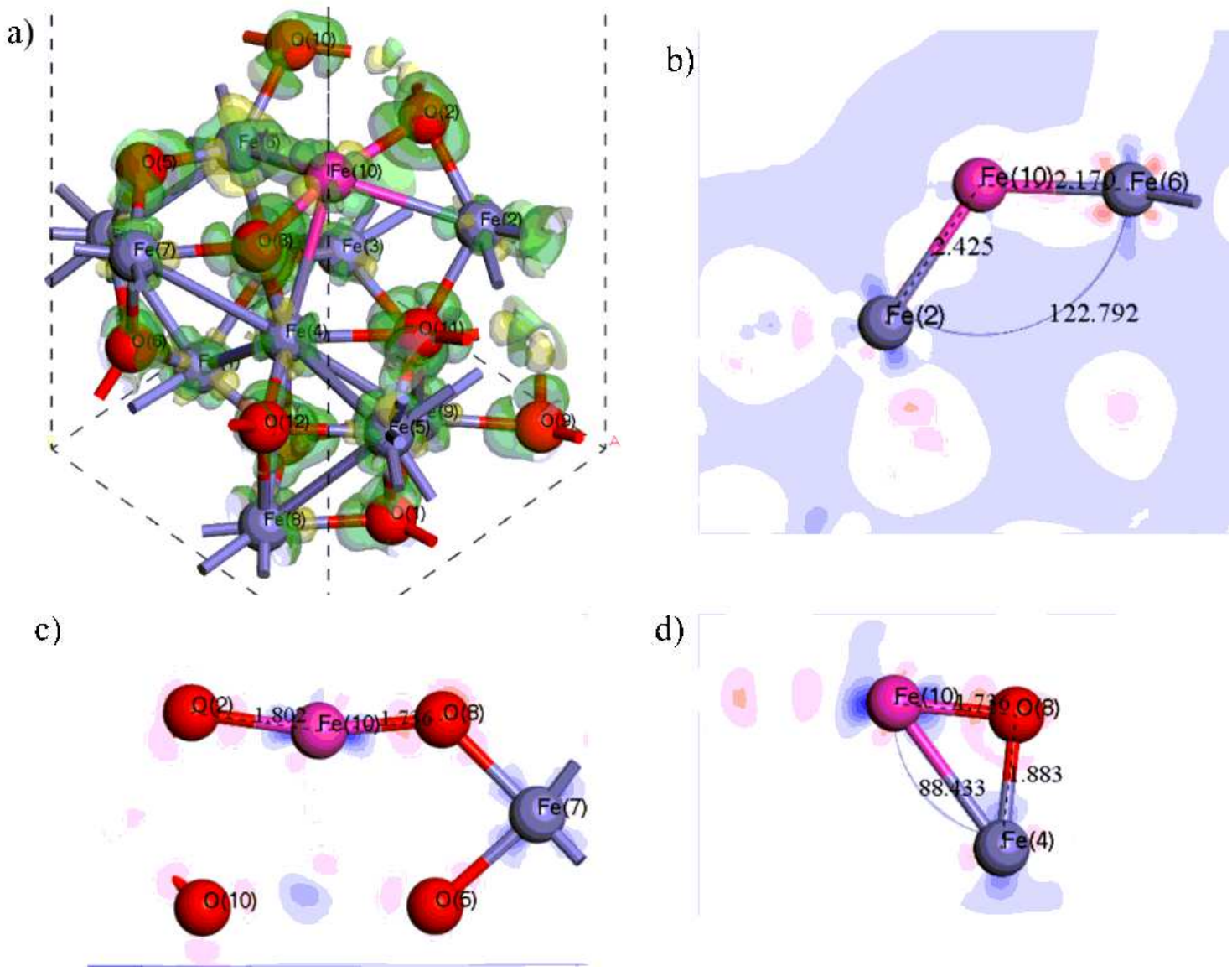

Figure 9

Please see the Manuscript Doc file for the complete figure caption.

Supplementary Files

This is a list of supplementary files associated with this preprint. Click to download.

- graphicabstract.pdf